

Recognizing the waveform of a foreshock

Eugenio Lippiello (✉ eugenio.lippiello@unicampania.it)

University of Campania <https://orcid.org/0000-0003-1444-1889>

Giuseppe Petrillo

University of Campania

Cataldo Godano

University of Campania

Article

Keywords: earthquake, foreshock, waveform

Posted Date: August 14th, 2020

DOI: <https://doi.org/10.21203/rs.3.rs-57209/v1>

License:  This work is licensed under a Creative Commons Attribution 4.0 International License.

[Read Full License](#)

Recognizing the waveform of a foreshock

Lippiello E.^{1,*}, Petrillo G.¹ & Godano C.^{1,2}

¹*Department of Mathematics and Physics, University of Campania “L. Vanvitelli”, 81100 Caserta, Italy.*

²*Istituto Nazionale Geofisica e Vulcanologia, Napoli, Italy.*

The 2011 Mw9.1 Tohoku, Japan, earthquake is the paradigmatic example of an earthquake anticipated by a significant foreshock activity, with a Mw7.3 earthquake occurred two days before, within about 10 km ¹. Recent results ² show that statistically relevant changes can be found in the magnitude distribution after the Mw7.3 foreshock but the discrimination between normal and foreshock activity still remains a scientific challenge ³. Here we show that the envelope of the ground velocity recorded after the Mw7.3 foreshock presents an atypical *sawtooth* profile very different from the one observed after other earthquakes ⁴. We interpret this profile as the consequence of the locked state of the mainshock fault which reduces the possibility of the foreshock to trigger its own aftershocks. We find a similar sawtooth profile after other Mw6+ foreshocks followed within 10 days by a larger earthquake, as in the case of the 2014 Mw8.1 Iquique, Chile, sequence. This observation allows us to define a level of concern, simply extracted from the first 45 minutes of the recording waveform, associated to the occurrence of a larger earthquake. A test of the method for 47 Mw6+ worldwide earthquakes gives precise warning in time and space after all the 10 earthquakes followed by a

larger one with only 2 false alerts.

1 The coseismic slip during a large earthquake causes a shear stress reduction in regions which
2 have experienced large slips and, at the same time, concentrates residual shear stress near the slip
3 zone margins ⁵. This stress redistribution promotes the occurrence of aftershocks with an abrupt
4 increase of the seismic rate. During normal activity the aftershock magnitudes get smaller for
5 increasing time, but, occasionally, aftershocks larger than the mainshock are observed. In these
6 cases the mainshock is relabeled foreshock, the largest earthquake becomes the mainshock and
7 the key question becomes if it is possible to distinguish foreshocks from normal seismic activity.
8 Focusing on moderate up to intermediate ($M_w < 5$) mainshock magnitudes, after the original pa-
9 per by Brodsky ⁶, several studies ⁷⁻¹² have shown that the number of foreshocks in instrumental
10 catalogs is larger than the one expected according to normal earthquake clustering models. This
11 result is also in agreement with a recent study ¹³, before $M_w 4$ mainshocks, which uses a high-
12 resolution earthquake catalog. Statistically relevant deviations from normal seismicity has been
13 also found ⁷ before $M_w 6+$ mainshocks but the first clear proof of the relevance of foreshocks in
14 improving the forecast of large ($M_w 6.5+$) mainshocks has been only recently obtained by Gu-
15 lia & Wiemer (GW) ². Indeed, GW demonstrated that the b -value of the Gutenberg-Richter (GR)
16 law decreases during foreshock activity whereas previous studies ¹⁴ have shown that it increases
17 during normal aftershock sequences. This pattern has been observed in the temporal interval of
18 two days separating the $M_w 7.3$ foreshock and the 2011 $M_w 9.1$ Tohoku mainshock. During the
19 same interval, episodic slow slip events have been observed ¹⁵⁻¹⁷ and they have been interpreted

20 as precursors according to the pre-slip model ^{18,19}. Other observations ²⁰, conversely, support the
21 cascade model ^{21,22} where foreshocks are no different from other sets of clustered earthquakes.

22 In this article we show that it is possible to discriminate between foreshocks and normal
23 seismic sequences from the profile of the envelope $\mu(t)$, defined as the logarithm of the envelope
24 of the ground velocity (see Methods). Immediately before an earthquake, $\mu(t)$ starts from the
25 background level μ_B and rapidly raises up to the time t_M , when it reaches its maximum value μ_M .
26 This value corresponds to the perceived magnitude close to the recording station and represents
27 the mainshock magnitude apart from an additive term. The presence of aftershocks is clearly
28 visible ^{4,23-26} in the decay of the envelope function $\mu(t)$, at times $t > t_M$. We present two limit
29 cases in Fig.1[1a]: The 2019/11/27 Mw6.1 Platanos earthquake followed by no aftershock and the
30 2017/07/20 Mw6.6 Kos earthquake with many aftershocks identified in the first hours ²⁷. After the
31 Mw6.1 Platanos earthquake, for times $t > t_M$, $\mu(t)$ fast decays and then remains stationary around
32 $\mu(t) \simeq \mu_B$. Conversely, after the Kos earthquake, $\mu(t)$ does not go back to μ_B but fluctuates around
33 a plateau with a minimum value μ_L significantly larger than μ_B . To understand the origin of the
34 plateau, we must take into account that if an aftershock has occurred at time t_1 , with perceived
35 magnitude μ_1 , it produces a peak $\mu(t_1) = \mu_1$ in the envelope. After this peak, $\mu(t)$ would decrease
36 towards μ_B but if an other aftershock with perceived magnitude μ_2 occurs at the time $t_2 > t_1$,
37 the envelope raises again reaching a second peak $\mu(t_2) = \mu_2$. If the aftershock productivity is
38 very high then the temporal distance $(t_2 - t_1)$ between two subsequent aftershocks is very short
39 and $\mu(t)$ is not able to decay below a level of the plateau $\mu_L \simeq \mu_2$. In particular, in ref. ²⁵ it was

40 numerically shown that the number of aftershocks exponentially increases by increasing $\mu_L - \mu_B$.
 41 More precisely, a very qualitative estimate indicates that the expected number of aftershocks (with
 42 $\mu_i > \mu_M - 2$) following a mainshock with perceived magnitude μ_M , is roughly proportional to
 43 $n_{aft} = 10^{-\delta\mu}$, with $\delta\mu = (\mu_M - \mu_B) - 2(\mu_L - \mu_B)$. A precise estimate of the aftershock occurrence
 44 probability from $\mu(t)$, in the first minutes after t_M , can be found in Ref. ⁴.

45 In Fig.1[1b] we plot $\mu(t)$ after the Mw7.3 2011/03/09 foreshock. According to the cascade
 46 model ^{21,22} the occurrence of an aftershock larger than the mainshock is a rare event which is more
 47 probable to occur during an intense aftershock activity. Accordingly, the normal behavior of the
 48 envelope function (Fig.1[1a]) would have suggested a high plateau level with a large value of n_{aft} .
 49 Instrumental data (black line in Fig.1[1b]), conversely, show exactly the opposite trend with $\mu(t)$
 50 reaching values close to μ_B about 8 minutes after the mainshock, similarly to the no-aftershock
 51 pattern observed after the Mw6.1 Platanos earthquake (Fig.1[1a]). At variance with the Platanos
 52 earthquake, in the case of the Mw7.3 Tohoku foreshock, after reaching the minimum value, the
 53 envelope $\mu(t)$ abruptly raises and then drops again to $\mu(t) \simeq \mu_B$ producing an anomalous *sawtooth*
 54 profile. The presence of large peaks corresponds to the occurrence of large foreshocks ($\mu_i \simeq$
 55 $\mu_B + 4$) whereas the presence of valleys with $\mu(t) \simeq \mu_B$ corresponds to temporal periods with very
 56 few $\mu_i > \mu_B$ earthquakes. Therefore $\mu(t)$ shows the existence of temporal periods of some minutes
 57 with zero events (valleys) interrupted by large earthquakes (peaks). This is incompatible with the
 58 GR law which predicts thousands of events with $\mu_i \simeq \mu_B + 1$ for each event with $\mu_i \simeq \mu_B + 4$.
 59 Looking at the envelope $\mu(t)$ after the Mw9.1 mainshock (red curve in Fig.1[1b]), conversely, we

60 find the normal profile with a high plateau level μ_L , as during standard aftershock triggering. The
61 same behavior is observed at different seismic stations (Suppl. Fig.3).

62 Summarizing, the sawtooth profile of $\mu(t)$ after the Mw7.3 Tohoku foreshock reveals a very
63 limited capability in triggering small aftershocks. A physical interpretation of this behavior, con-
64 sistent with the pre-slip model, is qualitatively illustrated in the cartoon of Fig.2a. The Tohoku
65 sequence has occurred in a region of the plate boundary which has not experienced a large earth-
66 quake for over a century and, according to geodetic data, the area of maximum coseismic slip was
67 probably locked for a period of several years before the foreshock ²⁹. It is then reasonable, consis-
68 tently with the asperity model ³⁰, that the accumulated elastic strain leads to the existence of a vast
69 and strongly correlated region along the plate (the red region in Fig.2a): A slip of a sub-region,
70 even small in size, inside the red area will produce the synchronized rupture of several asperities
71 with the global failure of the whole region. Nevertheless, because of frictional heterogeneities, it
72 is reasonable to expect the existence of weaker regions within the red area (blue regions in Fig.2a).
73 These regions are less locked and will achieve slip instabilities before the red one. Foreshocks are
74 caused by the coseismic slip of these (blue) regions leading to a stress concentration at their pe-
75 riphery, i.e. inside the red area. Within this interpretation, therefore, the occurrence of a foreshock
76 either will cause the global failure of the whole (red) area or can trigger aftershocks only inside
77 another blue region or outside the red region (green area in Fig.2a). In presence of a slow drive
78 process, other blue regions are brought close to failure and the envelope takes the form of isolated
79 peaks (foreshocks) separated by temporal periods of quasi-zero seismicity (valleys). This should

80 affect the peak distribution $P(\mu)$ (see Methods) which typically follows the Ishimoto-Iida law ²⁸
81 $P(\mu_i) \sim 10^{-\beta\mu_i}$, where β roughly coincides with the b -value of the GR law. Since the presence
82 of isolated foreshocks corresponds to a deficit of small events we should expect a smaller β -value.
83 We indeed measure a β -value ($\beta = 0.4 \pm 0.1$) after the Mw7.3 foreshock significantly smaller
84 than the value $\beta = 1.0 \pm 0.1$ after the Mw9.1 mainshock. The observed change in the β -value is
85 consistent with the one found by GW in the b -value ².

86 We next look for the anomalous behavior of $\mu(t)$, observed after the Mw7.3 Tohoku fore-
87 shock, after other earthquakes. We consider all Mw6+ events, occurred after 2010, followed within
88 10 days by a larger earthquake and recorded by a seismic station at distance smaller than ~ 100
89 km, with a level of the background signal $\mu_B \lesssim 1$, which is sufficiently low to indicate that the
90 envelope is weakly influenced by previous seismicity. There are 10 mainshocks, highlighted in
91 Suppl. Table 1, that match our criterion. We have investigated $\mu(t)$ after each mainshock and its
92 most relevant foreshocks (all shown in Sec.2 in the Supporting Information). We find that $\delta\mu$ after
93 the foreshocks is always larger than the same quantity after the corresponding mainshock. In par-
94 ticular, the anomalous sawtooth profile, observed after the Mw7.3 Tohoku foreshock, is also found
95 in other foreshocks when the foreshock hypocenter is located very close to the relative mainshock
96 one and therefore reasonably well inside the locked (red) area, as in the case of the 2014/03/23
97 Mw6.2 Iquique foreshock ³¹. The evolution of $\mu(t)$ then supports our interpretation (Fig.2a) and
98 confirms the sawtooth profile as a distinctive feature of foreshock activity.

99 Fig.2b schematically describes a different situation where the foreshock occurs on the border
100 of the locked (red) area. The 2014/03/14 Mw6.7 Iquique foreshock, the 2016/08/24 Mw6.2 Am-
101 atrice foreshock and the 2016/10/26 Mw6.1 Visso foreshock belong to this situation ^{31,34}. In this
102 case a fraction of the stress is redistributed within the “no-aftershock” red zone but the remaining
103 stress is concentrated within the green zone, leading to normal aftershock activity. In presence of
104 a slow driving process we therefore expect that foreshock activity within blue regions is superim-
105 posed to standard aftershock triggering outside the locked portion of the fault. We indeed observe
106 (green curve in Fig.1[1c]) that $\mu(t) - \mu_B$ drops to a small but significantly larger than zero value
107 and this can be attributed to a low but non null normal aftershock triggering. At the same time
108 we can easily identify the presence of some large isolated peak μ_i , which can be associated to the
109 foreshock occurrence. Fig.2c schematically describes a further different situation where the fore-
110 shock occurs on a secondary fault, close in space but different from the mainshock one, as for the
111 2019/07/04 Mw6.4 Ridgecrest foreshock ³⁵. Also in this case, as in the situation of Fig.2b, we ex-
112 pect the coexistence of normal aftershock activity along the secondary fault with foreshock activity
113 along the main fault. This should produce an hybrid behavior of $\mu(t)$ with a small but non null
114 value of $\mu_L - \mu_B$ and, at the same time, the presence of large quite isolated peaks μ_i , as confirmed
115 by instrumental data (green curve in Fig.1[1d]). Also the 2016/04/14 Mw6.2 Kumamoto foreshock
116 occurred on a secondary fault ³⁶ and $\mu(t)$ exhibits an hybrid behavior (Supp. Fig. 27). At the same
117 time, the Ridgecrest sequence presents a Mw5.4 foreshock occurred very close in space (epicentral
118 distance ~ 2 km) only 16 hours before the mainshock. This foreshock exhibits a profile of $\mu(t)$
119 more similar to the Mw7.3 Tohoku foreshock (black curve in Fig.1[1d]).

120 According to previous observations, foreshock activity exhibits a much larger number of
121 events n_{obs} with high peak values ($\mu_i > \mu_M - 2$) compared to its expected number n_{aft} . The
122 quantity n_{obs}/n_{aft} should be therefore exhibit abnormal large values during foreshock sequences
123 and $Q = (n_{obs}/n_{aft})10^{-\beta\mu_M}$ can be used to define the level of concern associated to the occurrence
124 of a subsequent earthquake with peak magnitude larger than μ_M (see Methods). We consider as
125 target earthquakes all Mw6+ earthquakes which, in the last decade, have been followed, within 10
126 days, by an earthquake with a larger value of μ_M . For comparison, we also take into account all
127 Mw6+ earthquakes occurred after 2015 in geographic regions with dense seismic stations (in-land
128 Japan, Central Europe and North America). Imposing a constraint on the quality of the recorded
129 waveform (see Methods) we collect a sample of 47 earthquakes listed in Suppl. Table 1 and
130 including 10 target earthquakes. To statistically validate our method we use the receiver operating
131 characteristic (ROC) diagram adopting a binary code which switches on the alarm when Q is larger
132 than a given threshold Q_{th} . By changing the value of Q_{th} we evaluate the fraction of true positive
133 rate (TPR), i.e. the number of events with $Q > Q_{th}$ and followed by a larger earthquake divided
134 by the total number of target earthquakes. We also evaluate the fraction of false alarm rate (FAR),
135 defined as the fraction of events with $Q > Q_{th}$ and NOT followed by a larger earthquake. By
136 changing Q_{th} we obtain a diagram (Fig.3) with points close to the perfect prediction ($TPR =$
137 $1, FAR = 0$) and well above the random prediction, which can be discarded with a confidence
138 level above the 99.99999%.

139 In Suppl. Fig.1 we show that there exists a specific $Q_{th} = 0.18$ which allows us to score all

140 the 10 successful alerts, with no missed events, two false alerts, and 35 correct negatives. Inter-
141 esting, this value of Q_{th} was identified at the time of the first submission and the two foreshocks
142 among the 7 earthquakes occurred later (last 7 events in Suppl. Table 1) are correctly discriminated
143 by the comparison between Q and $Q_{th} = 0.18$.

144 This result is obtained using $\beta = 1$ in the definition of Q , which leads to an expression of Q
145 only in terms of the quantities μ_B , μ_L and n_{obs} which can be easily obtained from the first minutes
146 of the envelope $\mu(t)$ (see Methods). This gives some advantages with respect to the GW method
147 (see Supplementary Materials) and allows us to overcome all the problems related to the estimate of
148 the b -value³. Indeed, the quantity Q is analogously defined for all earthquakes whereas the choice
149 of the normal b -value requests a decision-making specific for each earthquake. Furthermore, our
150 results are not affected by problems of aftershock completeness and we can therefore test the
151 model over an ensemble including up to 10 true positive cases. However, we wish to remark
152 that our method can provide information of the stress state of a fault only at the occurrence time
153 of a big foreshock. Indeed, the earthquake must be sufficiently large to distribute stress over
154 a wide region of the fault so to discriminate locked from unlocked regions (red and blue areas in
155 Fig.2). The evaluation of the b -value, conversely, provides the opportunity to monitor the evolution
156 of the stress on the fault over sufficiently long temporal periods as for instance in the case of
157 the Tohoku earthquake when a decreasing trend in the b -value has been documented for a period
158 of several years before the Mw7.3 foreshock³⁷. At the same time the b -value can be used to
159 identify the stress change induced by big foreshocks with results in substantial agreement with

160 the evaluation of Coulomb stress changes ³⁸. As a consequence it appears reasonable that one can
161 achieve more accurate forecasting by combining the two approaches: the Q value can be adopted as
162 an initial discriminant and the b -value can be used to identify higher stressed regions, which will be
163 probably host the subsequent mainshock. Nevertheless, in the Kumamoto sequence the b -value has
164 increased in the surrounding of the future mainshock hypocenter ³⁹. As an example of combining
165 the two approaches we observe that, consistently with the GW prediction of small b -values during
166 foreshock activity, the peak distribution $P(\mu)$ (upper panels of Fig.1[2a-2d] and Suppl. Table.1)
167 presents atypical small values of $\beta \leq 0.74$ after the foreshocks compared to larger values of β
168 observed after the mainshocks. Implementing in the definition of Q the β value extracted from
169 $P(\mu)$, we find an even clearer discrimination of foreshock from normal aftershock activity (Fig.3
170 and Suppl. Fig.2) with just one false alert.

171 Summarizing, we present a simple procedure which can be used to characterize the stress
172 state of a fault and can help local authorities in the management of post-seismic risk.

173 **Methods**

174 **The envelope function**

175 We filter the vertical component of the ground velocity in the range $[2, 10]$ Hz, we apply
176 a Hilbert transformation and we take the logarithm to base 10. We finally define the envelope
177 function $\mu(t)$ after applying a smoothing procedure on a moving window including 5 points. We

178 find very similar results using the two horizontal components and different choices of the frequency
179 range. Only for graphical purposes, in Fig.1 we extend the smoothing procedure to a moving
180 window of 200 points.

181 **The evaluation of Q**

182 We define the quantity t_M as the time such that $\mu(t)$ takes its maximum value and the per-
183 ceived magnitude is $\mu_M = \mu(t_M)$. We define the quantity μ_B as the minimum value of $\mu(t)$ in the
184 temporal window $[t_M - \Delta t_B, t_M]$ and μ_L as the minimum value of $\mu(t)$ in the temporal window
185 $[t_M, t_M + \Delta t_L]$. In our study we consider $\Delta t_B = 400$ sec and $\Delta t_L = 45$ min. We have verified
186 that similar results are obtained for $\Delta t_B \in [2, 10]$ min and $\Delta t_L \in [30, 60]$ min. We take the signal
187 recorded at the station with the smallest value of μ_B and in all cases we always consider waveforms
188 with $\mu_B \leq 1$. At the same time we only take into account waveforms with a perceived magnitude
189 $\mu_M \geq 5$. Since μ_M is the decreasing function of the epicentral distance of the recording station
190 we usually consider the closest station compatible with the above constraint on μ_B . We have also
191 verified that the value of μ_M is not affected by saturation problems.

192 **The selection of earthquakes**

193 We adopt the searching criterion of the USGS earthquake hazard program to obtain the occur-
194 rence time and epicentral coordinates of an Mw6+ earthquake. We next consider regional networks
195 to verify this information and to identify the stations closest to the earthquake epicenter. Once the

196 waveform with the ground velocity has been downloaded, the procedures to obtain the envelope
197 and to evaluate Q , illustrated above, are automatically implemented.

198 **The peak distribution**

199 We identify aftershocks from the envelope function $\mu(t)$ by means of the procedure devel-
200 oped by Peng et al. ²³. We define the quantity n_{obs} as the number of aftershocks producing a peak
201 magnitude $\mu_i \geq \mu_M - 2$ in the temporal interval $[t_M + 300sec, t_M + \Delta t_L]$. We remove the first
202 300 seconds from this analysis since, in this time window, aftershocks can be hidden by the coda
203 wave of the main event. We evaluate of the peak distribution $P(\mu)$ extending the temporal inter-
204 val to 1 day, $t \in [t_M + 300sec, t_M + 1day]$ and the β -value is given by the best exponential fit
205 $P(\mu) = A10^{-\beta\mu}$ for $\mu > \mu_M - 2$, according to the Ishimoto-Iida law.

1. Hirose, F., Miyaoka, K., Hayashimoto, N., Yamazaki, T. & Nakamura, M. Outline of the 2011 off the pacific coast of Tohoku earthquake (Mw 9.0) seismicity: foreshocks, mainshock, aftershocks, and induced activity. *Earth, Planets and Space* **63** (2011).
2. Gulia, L. & Wiemer, S. Real-time discrimination of earthquake foreshocks and aftershocks. *Nature* **574**, 193–199 (2019).
3. Brodsky, E. Predicting if the worst earthquake has passed. *Nature* **574**, 185–186 (2019).
4. Lippiello, E. *et al.* Forecasting of the first hour aftershocks by means of the perceived magnitude. *Nature Communications* **10**, 2953 (2019).

5. Wetzler, N., Lay, T., Brodsky, E. E. & Kanamori, H. Systematic deficiency of aftershocks in areas of high coseismic slip for large subduction zone earthquakes. *Science Advances* **4** (2018).
6. Brodsky, E. E. The spatial density of foreshocks. *Geophysical Research Letters* **38**, L10305 (2011). L10305.
7. Lippiello, E., Marzocchi, W., de Arcangelis, L. & Godano, C. Spatial organization of foreshocks as a tool to forecast large earthquakes. *Sci. Rep.* **2**, 1–6 (2012).
8. Shearer, P. M. Self-similar earthquake triggering, Bath’s law, and foreshock/aftershock magnitudes: Simulations, theory, and results for Southern California. *Journal of Geophysical Research-Solid Earth* **117**, (2012).
9. Ogata, Y. & Katsura, K. Comparing foreshock characteristics and foreshock forecasting in observed and simulated earthquake catalogs. *Journal of Geophysical Research: Solid Earth* **119**, 8457–8477 (2014). 2014JB011250.
10. de Arcangelis, L., Godano, C., Grasso, J. R. & Lippiello, E. Statistical physics approach to earthquake occurrence and forecasting. *Physics Reports* **628**, 1 – 91 (2016).
11. Lippiello, E., Giacco, F., Marzocchi, W., Godano, C. & Arcangelis, L. d. Statistical features of foreshocks in instrumental and ETAS catalogs. *Pure and Applied Geophysics* 1–19 (2017).

12. Seif, S., Zechar, J. D., Mignan, A., Nandan, S. & Wiemer, S. Foreshocks and Their Potential Deviation from General Seismicity. *Bulletin of the Seismological Society of America* **109**, 1–18 (2018).
13. Trugman, D. T. & Ross, Z. E. Pervasive foreshock activity across Southern California. *Geophysical Research Letters* **46**, 8772–8781 (2019).
14. Gulia, L. *et al.* The effect of a mainshock on the size distribution of the aftershocks. *Geophysical Research Letters* **45**, 13,277–13,287 (2018).
15. Ito, Y. *et al.* Episodic slow slip events in the Japan subduction zone before the 2011 Tohoku-Oki earthquake. *Tectonophysics* **600**, 14 – 26 (2013). Great Earthquakes along Subduction Zones.
16. Kato, A. *et al.* Propagation of slow slip leading up to the 2011 Mw 9.0 Tohoku-Oki earthquake. *Science* **335**, 705–708 (2012).
17. Brodsky, E. E. & Lay, T. Recognizing foreshocks from the 1 april 2014 Chile earthquake. *Science* **344**, 700–702 (2014).
18. Ellsworth, W. L. & Beroza, G. C. Seismic evidence for an earthquake nucleation phase. *Science* **268**, 851–855 (1995).
19. Dodge, D. A., Beroza, G. C. & Ellsworth, W. L. Detailed observations of California foreshock sequences: Implications for the earthquake initiation process. *Journal of Geophysical Research: Solid Earth* **101**, 22371–22392 (1996).

20. Marsan, D. & Enescu, B. Modeling the foreshock sequence prior to the 2011, Mw9.0 Tohoku, Japan, earthquake. *Journal of Geophysical Research: Solid Earth* **117** (2012).
21. Fukao, Y. & Furumoto, M. Hierarchy in earthquake size distribution. *Physics of the Earth and Planetary Interiors* **37**, 149 – 168 (1985).
22. Helmstetter, A. & Sornette, D. Foreshocks explained by cascades of triggered seismicity. *Journal of Geophysical Research: Solid Earth* **108**, 2457 (2003).
23. Peng, Z., Vidale, J. E., Ishii, M. & Helmstetter, A. Seismicity rate immediately before and after main shock rupture from high-frequency waveforms in Japan. *Journal of Geophysical Research: Solid Earth* **112**, n/a–n/a (2007).
24. Sawazaki, K. & Enescu, B. Imaging the highfrequency energy radiation process of a main shock and its early aftershock sequence: The case of the 2008 Iwate Miyagi Nairiku earthquake, Japan. *Journal of Geophysical Research: Solid Earth* **119**, 4729–4746 (2014).
25. Lippiello, E., Cirillo, A., Godano, G., Papadimitriou, E. & Karakostas, V. Real-time forecast of aftershocks from a single seismic station signal. *Geophysical Research Letters* **43**, 6252–6258 (2016). 2016GL069748.
26. Lippiello, E., Cirillo, A., Godano, C., Papadimitriou, E. & Karakostas, V. Post seismic catalog incompleteness and aftershock forecasting. *Geosciences* **9**, 355 (2019).

27. Karakostas, V., Papadimitriou, E., Mesimeri, M., & Begum, C. The 2017 Kos sequence: Aftershocks relocation and implications for activated fault segments. *36th ESC General Assembly, Valetta, Malta*, ESC2018-S6-645 (2018).
28. Ishimoto, M. & Iida, K. Observations sur les seismes enregistres par le microsismographe construit dernièrement. *Bulletin of the Earthquake Research Institute* **17**, 443–478 (1939).
29. Ikuta, R., Satomura, M., Fujita, A., Shimada, S. & Ando, M. A small persistent locked area associated with the 2011 Mw9.0 Tohoku-Oki earthquake, deduced from GPS data. *Journal of Geophysical Research: Solid Earth* **117** (2012).
30. Lay, T. & Kanamori, H. *An Asperity Model of Large Earthquake Sequences*, 579–592 (American Geophysical Union (AGU), 2013).
31. Ruiz, S. *et al.* Intense foreshocks and a slow slip event preceded the 2014 Iquique Mw 8.1 earthquake. *Science* **345**, 1165–1169 (2014).
32. Nealy, J. L. *et al.* 2017 Valparaso earthquake sequence and the megathrust patchwork of central Chile. *Geophysical Research Letters* **44**, 8865–8872 (2017).
33. Liu, S., Tang, C., Chen, C. & Xu, R. Spatiotemporal evolution of the 2018 Mw 6.4 Hualien Earthquake Sequence in Eastern Taiwan. *Seismological Research Letters* **90**, 1446–1456 (2019).

34. Improta, L. e. a. Multi-segment rupture of the 2016 Amatrice-Visso-Norcia seismic sequence (central Italy) constrained by the first high-quality catalog of early aftershocks. *Scientific Reports* **9** (2019).
35. Ross, Z. E. *et al.* Hierarchical interlocked orthogonal faulting in the 2019 Ridgecrest earthquake sequence. *Science* **366**, 346–351 (2019).
36. Yue, H. *et al.* The 2016 Kumamoto Mw = 7.0 earthquake: A significant event in a fault-volcano system. *Journal of Geophysical Research: Solid Earth* **122**, 9166–9183 (2017).
37. Nanjo, K. Z., Hirata, N., Obara, K. & Kasahara, K. Decade-scale decrease in b value prior to the M9-class 2011 Tohoku and 2004 Sumatra quakes. *Geophysical Research Letters* **39** (2012).
38. Nanjo, K. Were changes in stress state responsible for the 2019 Ridgecrest, California, earthquakes? *Nature Communications* **11**, 3082 (2020).
39. Nanjo, K. Z. & Yoshida, A. Anomalous decrease in relatively large shocks and increase in the p and b values preceding the April 16, 2016, M7.3 earthquake in Kumamoto, Japan. *Earth Planets Space* **69**, 13 (2017).

Author contributions E.L. conceived the study, data analysis has been performed by G.P and E.L. All authors have contributed to write the manuscript.

Competing Interests The Authors declare no competing interests.

Materials & Correspondence Correspondence and material requests can be addressed to E.L. (eugenio.lippiello@unicampania.it).

Acknowledgements We thank Eleftheria Papadimitriou and Vassilios Karakostas (Aristotle University of Thessaloniki) for data of Greek mainshocks. We thank the facilities of IRIS Data Services, and specifically the IRIS Data Management Center, were used for access to waveforms, related metadata, and/or derived products used in this study. IRIS Data Services are funded through the Seismological Facilities for the Advancement of Geoscience and EarthScope (SAGE) Proposal of the National Science Foundation under Cooperative Agreement EAR-1261681. We thank the National Research Institute for Earth Science and Disaster Resilience (2019), NIED Hi-net, National Research Institute for Earth Science and Disaster Resilience, doi:10.17598/NIED.0003, for data of the Tohoku sequence. We thank the GEOFON Data Centre (1993): GEOFON Seismic Network. Deutsches GeoForschungsZentrum GFZ. Other/Seismic Network. doi:10.14470/TR560404, for data of the Iquique sequence. We thank the Institute of Earth Sciences, Academia Sinica, Taiwan, for data of the Hualien sequence. This research activity has been supported by the Program VANviteLli pEr la RicErca: VALERE 2019, financed by the University of Campania "L. Vanvitelli. We also acknowledge support from MIUR-PRIN project "Coarse-grained description for non-equilibrium systems and transport phenomena (CO-NEST)" no. 201798CZL.

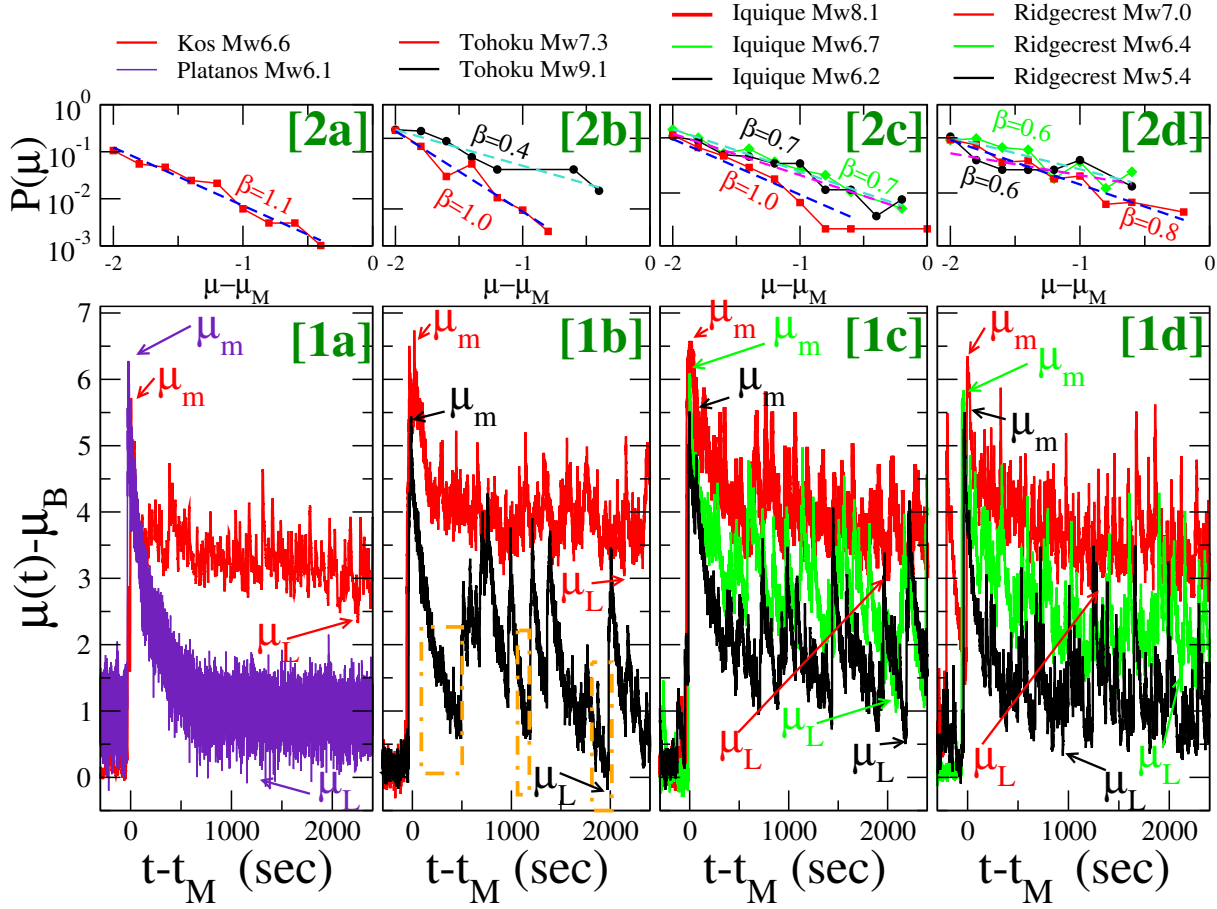


Figure 1: **The envelope function and the peak distribution.** The envelope function $\mu(t)$ is plotted as function of the time $t - t_M$ in the lower panels [1a-1d] and the corresponding peak distribution $P(\mu)$ is plotted in the upper panels [2a-2d]. Dashed lines in the upper panels are the exponential distribution $P(\mu) \propto 10^{-\beta\mu}$ and different colors correspond to the different best-fit β values. In panels [1a,2a] we consider two 'extreme' situations of normal aftershock triggering: The 2018 Mw6.6 Kos earthquake followed by a huge number of aftershocks (red curve [1a] and red squares [2a]) and the 2019 Mw6.1 Platanos earthquake followed by zero ($\mu_i > \mu_B$) aftershocks (violet curve [1a]). In panels [1b,2b] we consider the 2011 Tohoku sequence. Red line (lower panel) and red squares (upper panel) are used for the Mw9.1 mainshock. Black line (lower panel) and black circles (upper panel) are used for the Mw7.3 foreshock. The orange dot-dashed rectangles identify temporal periods with no $\mu_i > \mu_B + 1$ aftershock.

Figure 1: In panels [1c,2c] we consider the *2014 Iquique* sequence. Red line (lower panel) and red squares (upper panel) are used for the Mw8.1 mainshock. Green line (lower panel) and green diamonds (upper panel) are used for the Mw6.7 foreshock. Black line (lower panel) and black circles (upper panel) are used for the Mw6.2 foreshock. In panels [1d,2d] we consider the *2019 Ridgecrest* sequence. Red line (lower panel) and red squares (upper panel) are used for the Mw7.0 mainshock. Green line (lower panel) and green diamonds (upper panel) are used for the Mw6.4 foreshock. Black line (lower panel) and black circles (upper panel) are used for the Mw5.4 foreshock

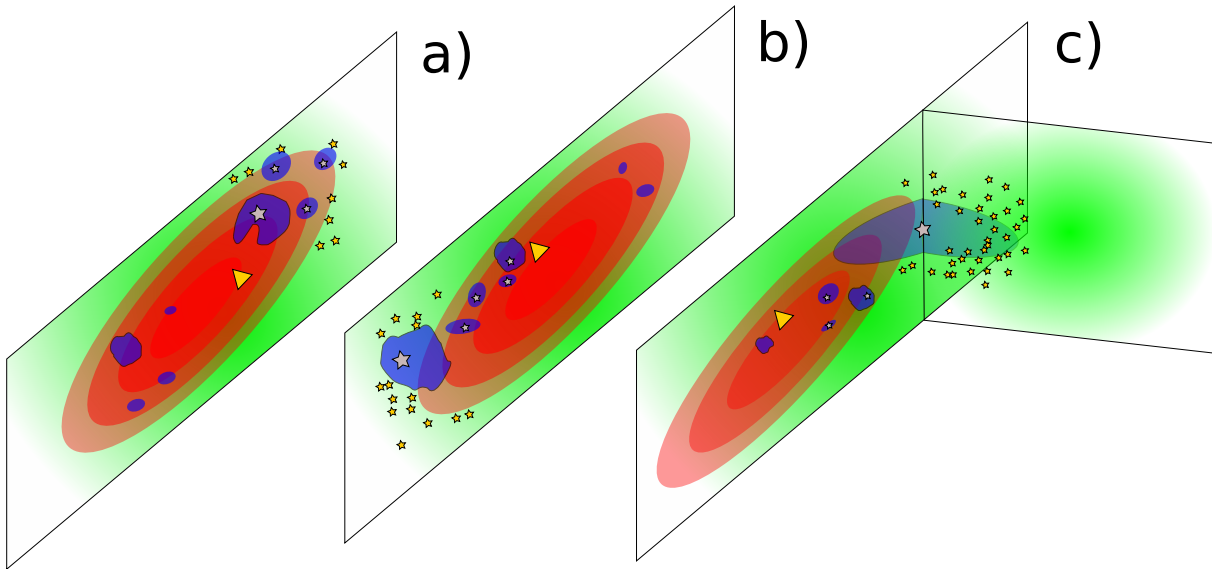


Figure 2: **Schematic description of the stress condition on the fault plane.** The color code indicates the degree of coupling of different regions on the fault plane, with deep red indicating very locked regions whereas light green indicates less coupled regions. The blue color indicates less locked region, inside the locked (red) area, where foreshock nucleation takes place. Grey stars, yellow stars and yellow triangles indicate the position of the epicenter of foreshocks, aftershocks and of the mainshock, respectively. Different panels schematically represent different scenarios, for the occurrence of the largest foreshock, qualitatively similar to the instrumental fore-mainshock sequences considered in Fig.1[1b-1d].

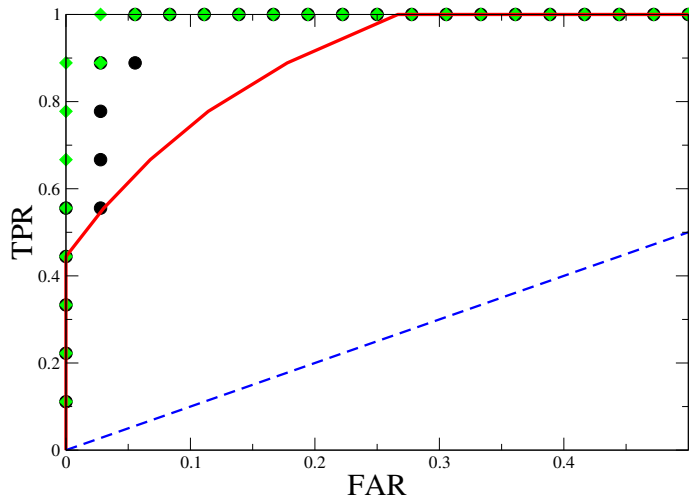


Figure 3: **The ROC diagram.** The true positive rate (TPR) is plotted versus the false alarm rate (FAR) for the method based on the Q -value with $\beta = 1$ (black circles) and with β extracted from data (green diamonds). The dashed blue diagonal represents random prediction (the null-hypothesis) whereas for points above the continuous red line, the null hypothesis can be rejected with a confidence level larger than 99.99999%.

Figures

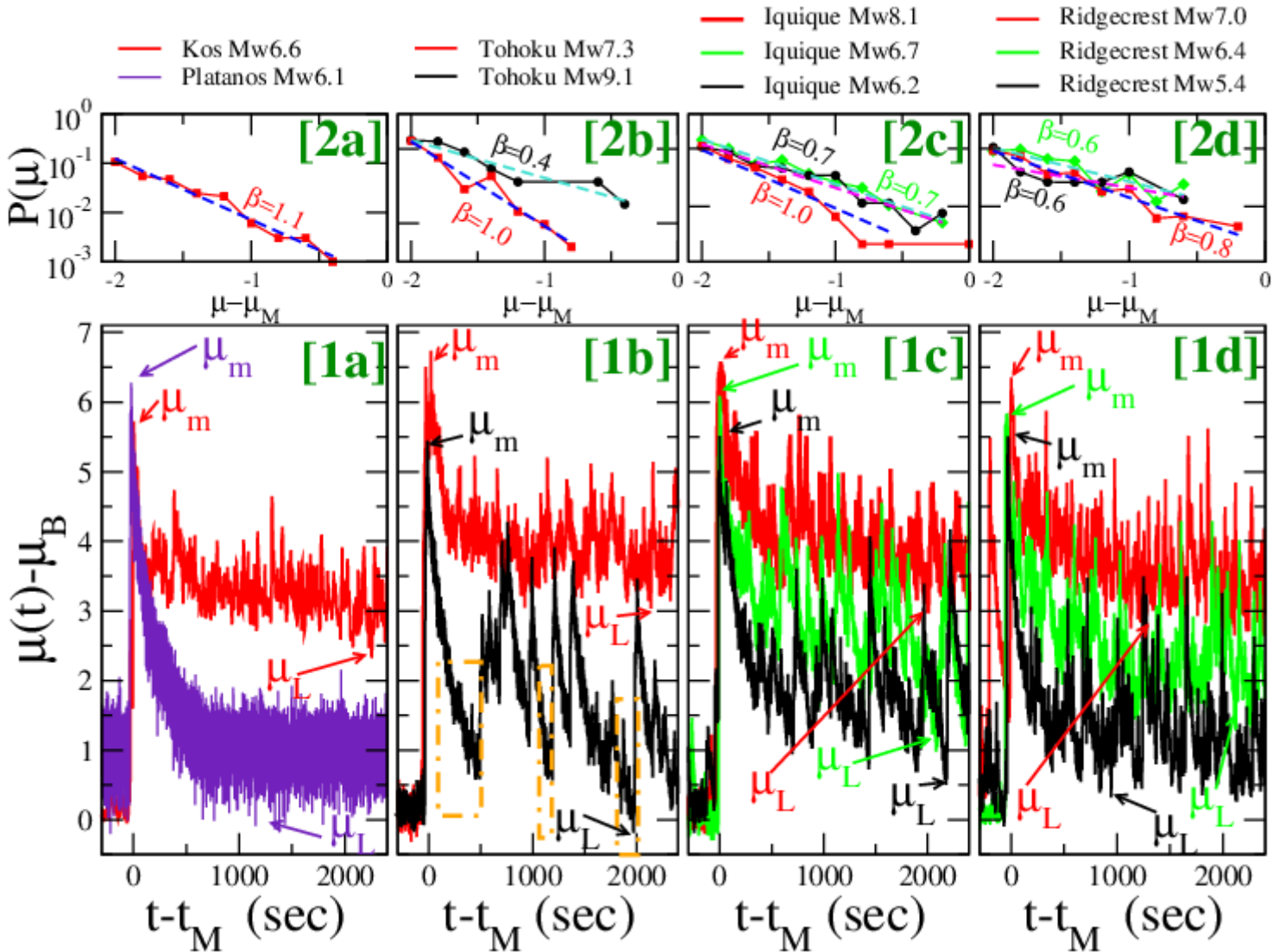


Figure 1

The envelope function and the peak distribution. The envelope function $\mu(t)$ is plotted as function of the time $t - t_M$ in the lower panels [1a-1d] and the corresponding peak distribution $P(\mu)$ is plotted in the upper panels [2a-2d]. Dashed lines in the upper panels are the exponential distribution $P(\mu) \propto 10^{-\beta\mu}$ and different colors correspond to the different best-fit β values. In panels [1a,2a] we consider two 'extreme' situations of normal aftershock triggering: The 2018 Mw6.6 Kos earthquake followed by a huge number of aftershocks (red curve [1a] and red squares [2a]) and the 2019 Mw6.1 Platanos earthquake followed by zero ($\mu_i > \mu_B$) aftershocks (violet curve [1a]). In panels [1b,2b] we consider the 2011 Tohoku sequence. Red line (lower panel) and red squares (upper panel) are used for the Mw9.1 mainshock. Black line (lower panel) and black circles (upper panel) are used for the Mw7.3 foreshock. The orange dot-dashed rectangles identify temporal periods with no $\mu_i > \mu_B + 1$ aftershock. In panels [1c,2c] we consider the 2014 Iquique sequence. Red line (lower panel) and red squares (upper panel) are used for the Mw8.1 mainshock. Green line (lower panel) and green diamonds (upper panel) are used for the Mw6.7

foreshock. Black line (lower panel) and black circles (upper panel) are used for the Mw6.2 foreshock. In panels [1d,2d] we consider the 2019 Ridgecrest sequence. Red line (lower panel) and red squares (upper panel) are used for the Mw7.0 mainshock. Green line (lower panel) and green diamonds (upper panel) are used for the Mw6.4 foreshock. Black line (lower panel) and black circles (upper panel) are used for the Mw5.4 foreshock

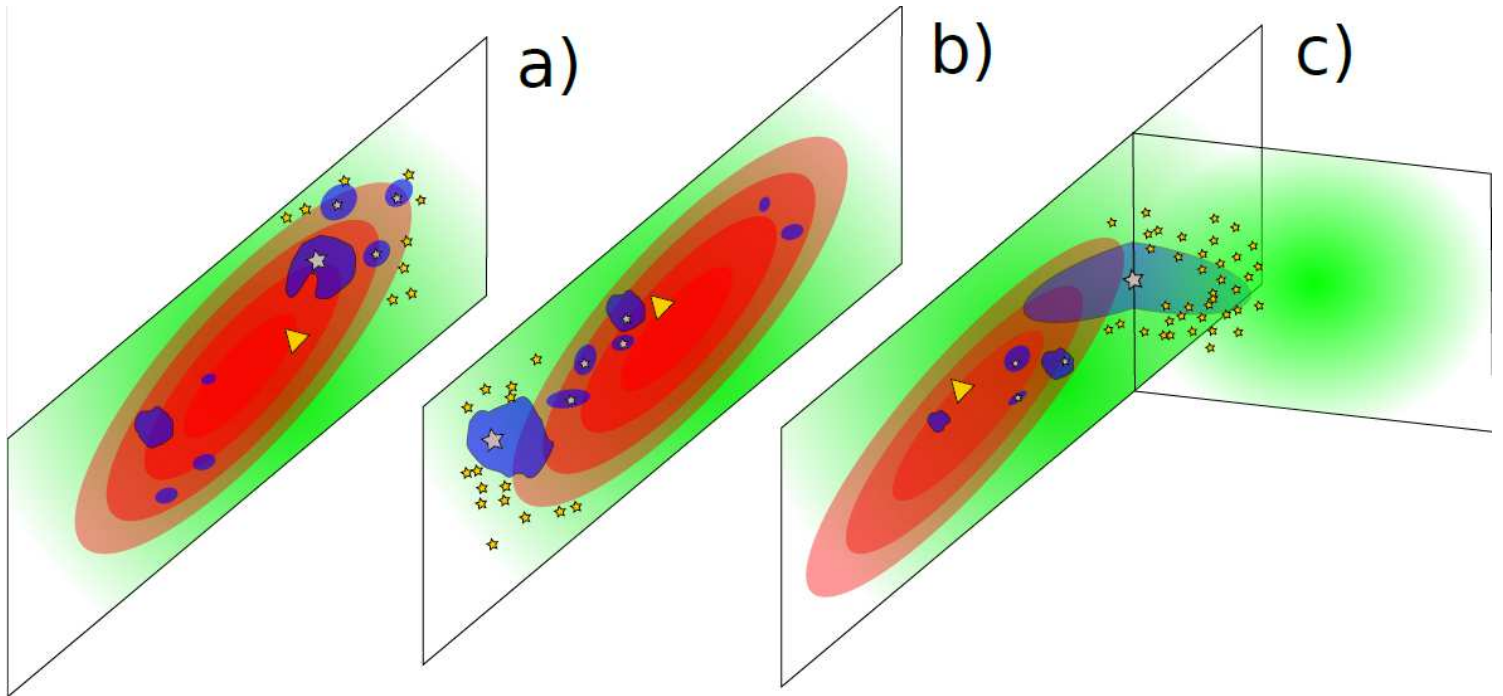


Figure 2

Schematic description of the stress condition on the fault plane. The color code indicates the degree of coupling of different regions on the fault plane, with deep red indicating very locked regions whereas light green indicates less coupled regions. The blue color indicates less locked region, inside the locked (red) area, where foreshock nucleation takes place. Grey stars, yellow stars and yellow triangles indicate the position of the epicenter of foreshocks, aftershocks and of the mainshock, respectively. Different panels schematically represent different scenarios, for the occurrence of the largest foreshock, qualitatively similar to the instrumental fore-mainshock sequences considered in Fig.1[1b-1d].

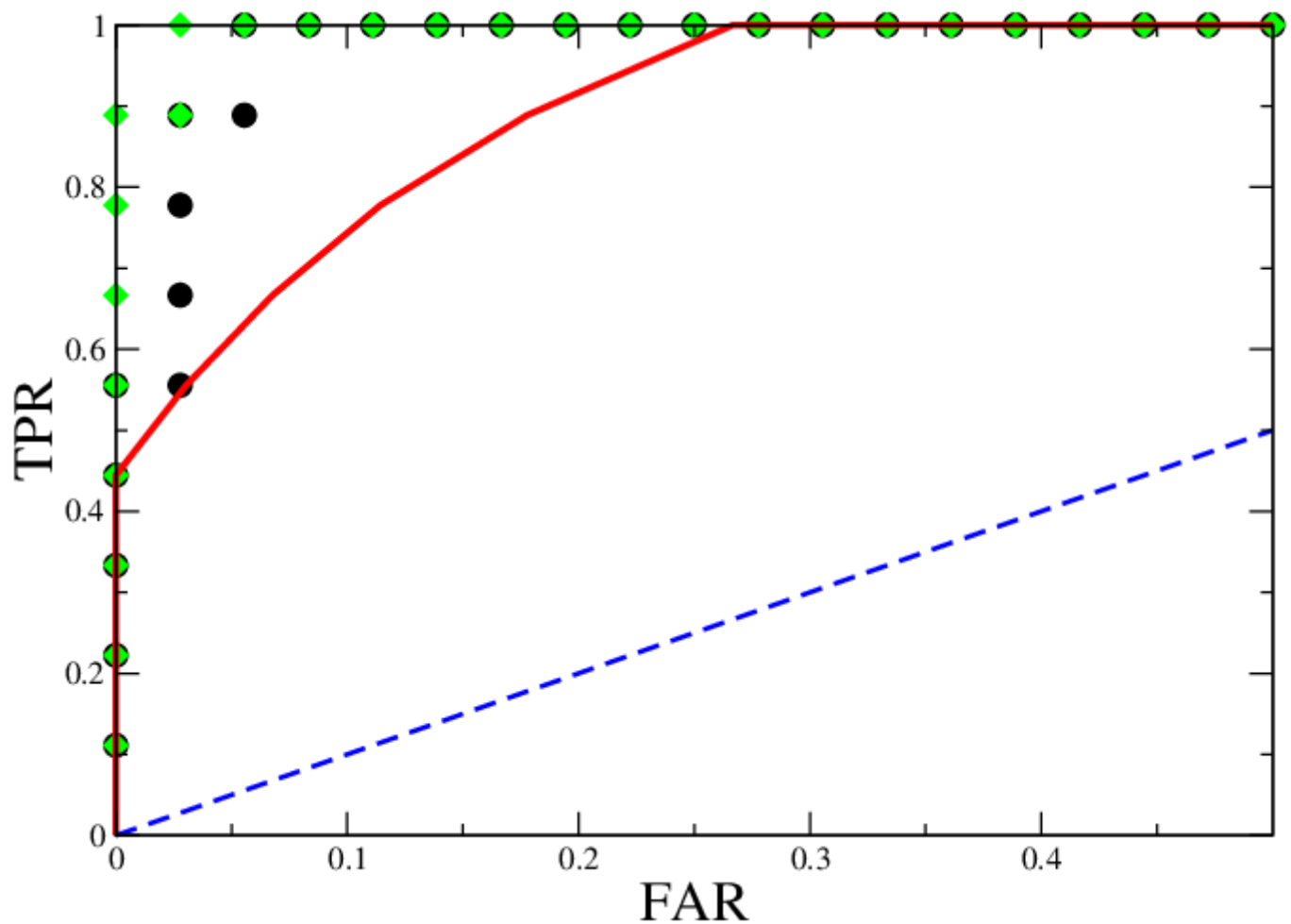


Figure 3

The ROC diagram. The true positive rate (TPR) is plotted versus the false alarm rate (FAR) for the method based on the Q-value with $\alpha = 1$ (black circles) and with α extracted from data (green diamonds). The dashed blue diagonal represents random prediction (the null hypothesis) whereas for points above the continuous red line, the null hypothesis can be rejected with a confidence level larger than 99:99999%.

Supplementary Files

This is a list of supplementary files associated with this preprint. Click to download.

- [supplem3.pdf](#)